Cytometry 31:275–286 (1998)

Original Articles

Efficient, Interactive, and Three-Dimensional Segmentation of Cell Nuclei in Thick Tissue Sections

Stephen J. Lockett,[1]* Damir Sudar,[1] Curtis T. Thompson,[2] Dan Pinkel,[1] and Joe W. Gray[1]

[1]Life Sciences Division, Ernest Orlando Lawrence Berkeley National Laboratory, Berkeley, California
[2]Department of Pathology, University of New Mexico, Albuquerque, New Mexico

Received 19 May 1997; Accepted 9 November 1997

Segmentation of intact cell nuclei in three-dimensional (3D) images of thick tissue sections is an important basic capability necessary for many biological research studies. Because automatic algorithms do not correctly segment all nuclei in tissue sections, interactive algorithms may be preferable for some applications. Existing interactive segmentation algorithms require the analyst to draw a border around the nucleus under consideration in all successive two-dimensional (2D) planes of the 3D image. The present paper describes an algorithm with two main advantages over the existing method. First, the analyst draws borders only in 2D planes that cut approximately through the center of the nucleus under consideration so that the nuclear borders generally are most distinct. Second, the analyst draws only five borders around each nucleus, and then the algorithm interpolates the entire surface. The algorithm results in segmented objects that correspond to individual, visually identifiable nuclei. The segmented surfaces, however, may not exactly represent the true nuclear surface. An optional, automatic surface optimization algorithm can be applied to reduce this error. Cytometry 31:275–286, 1998. © 1998 Wiley-Liss, Inc.

Key terms: interactive segmentation; confocal microscopy; tissue analysis

The combination of traditional histological analysis and the ability to measure characteristics of individual cells at the molecular level has proved to be very powerful for studies of normal biology and of disease states such as cancer. For example, in cancer, heterogeneity exists among the tumor cells and so requires analysis at the individual cell level. In addition, the relationship of the genotype of a cell to its phenotype may depend on its microenvironment (15). Usually such studies use tissue sections of 4 μm in thickness. Although this is often adequate, it cannot provide high accuracy for quantification because only partial cells are contained in the section. For example, using in situ hybridization (ISH) to measure the copy number of a specific genetic loci in each cell in the specimen underestimates the true count per cell because of truncation of the nuclei by sectioning. Similarly, measurement of the DNA content of cell nuclei in thin sections is grossly underestimated for large nuclei such as megakaryocytes and the Reed-Sternberg cells in Hodgkin's disease (7). Such problems can be largely overcome by using thick (≥20 μm) tissue specimens that contain mainly intact nuclei (17, 37). However, this requires the use of fluorescence labels so that the specimen remains largely transparent and the staining throughout the tissue volume can be detected by three-dimensional (3D; confocal) microscopy.

Extraction of quantitative measurements from confocal images of fluorescence labeled specimens is difficult, especially when the desired measurements are calculated from the intensity values of the image's voxels. It requires preparation of the specimen so that labeling of the specific molecular species is stoichiometric, and photobleaching, absorption and scattering of light, background from nonspecific labeling, and autofluorescence are minimized. It also requires careful selection of the objective lens to minimize spherical aberrations (caused by a refractive index difference between the specimen and medium between the specimen and lens) and which manifest

Contract grant sponsor: Office of Energy Research, Office of Health and Environmental Research of the U.S. Department of Energy; Contract grant number: DE-AC03-76SF00098; Contract grant sponsor: NIH; Contract grant number: CA-67412.

*Correspondence to: Stephen J. Lockett, M.S. 74-157, Lawrence Berkeley National Laboratory, 1 Cyclotron Road, Berkeley, CA 94720.
E-mail: sjlockett@lbl.gov

themselves as a worsening point spread function (PSF) and lower signal intensity as a function of increasing focal depth in the specimen. In addition, the lens should be color corrected for the excitation and emission wavelengths used and flat-field corrected across the field of view corresponding to the acquired image. When acquiring the image, a careful balance of light exposure to the specimen versus photobleaching must be achieved so that the signal-to-noise ratio (SNR) is maximal over the imaged volume.

After acquiring the images, analysis must be performed to extract the quantitative measurements. In studies in which accurate measurements are necessary, this may require prior preprocessing of the images. For example, in studies of chromatin texture, Strasters et al. (33) first had to deconvolve their images to remove the degradation caused by the PSF of the microscope and then to correct them for depth-associated absorption and scattering of the signal (34). This was followed by two image analysis steps: the first was accurate delineation of each nucleus and the second was measurement of the chromatin organization for each nucleus.

The ability to segment cell nuclei inside thick tissue sections is a valuable technique because of the wide range of biological questions it could help address, especially in cancer research, where cells in solid tumors are heterogeneous and their behavior likely depends on their environment (15). Consequently, there have been many attempts to segment nuclei from 3D images. This can be done either by automatic or by interactive algorithms.

Automatic algorithms have the advantage that thousands of nuclei can be segmented with little human effort. However, their performance is not completely accurate and depends on the specimen. In general, when nuclei are well separated and approximately spherical in shape, automatic algorithms work well. For example, Ancin et al. (1) applied an automatic 3D segmentation algorithm to 30-μm rat liver sections in which nuclei were not densely packed, and thus they could correctly segment 92% of the nuclei; however, for more irregular and more clustered nuclei, performance deteriorated. Rigaut et al. (29) reported similar results; they could automatically segment rat lived nuclei, but not nuclei in 60-μm sections of human in situ carcinoma of the esophagus. Another example of the difficulties of automatic segmentation has been reported by Mackin et al. (21) who found that the discrepancy between the number of cells counted manually versus automatically was up to 30% in regions of cervical smears that would have been ignored in two-dimensional (2D) imaging, presumably because of clustering of the cells. Even in studies in which there is one nucleus per 3D image, automatic segmentation may not be completely correct. This was found to be the case by Strasters et al. (33), who could only segment 66% of nuclei with their automatic procedure. The remaining 34% were segmented by a combination of fine tuning numerous parameters in their procedure and manual editing, leading the researchers to conclude that the segmentation problem is not yet solved.

Segmentation algorithms applied to cellular and medical images are evaluated by comparison with the visual interpretation of a human expert; thus, the only way to achieve complete accuracy is if the algorithm exactly matches the method used by the human eye–brain image analysis system. Automatic algorithms are a long way from this goal, but such performance can be achieved by interactive algorithms. As far as we are aware, the only existing 3D interactive segmentation algorithm for nuclei requires the analyst to draw a border around each nucleus under consideration in all successive 2D (xy) planes of a 3D image that contain the nucleus. This method has the advantage of virtually no restrictions on size, shape, or topology of the nuclei, but it is extremely time consuming when the nucleus spans more than a few optical sections (7,29). Furthermore, because of significant blurring in the z direction, it is especially difficult to determine the surfaces of nuclei in the z direction from only xy section views when nuclei are closely packed. This problem was experienced by Ancin et al. (1) who could not fully assess the accuracy of an automatic segmentation algorithm because it was impossible to determine by visual inspection of the images exactly how many nuclei were present.

In the present study, we overcame the disadvantages of interactive segmentation by developing a more efficient and more accurate interactive segmentation algorithm for nuclei. Greater efficiency was achieved by limiting to five the number of borders drawn around each nucleus. Greater accuracy was achieved by only drawing borders in planes that cut approximately through the center of the nuclei so that borders were generally most distinct.

METHODS

Interactive Algorithm for Segmenting Nuclei in 3D Images

The algorithm was written in C language as an extension to the SCIL_Image software package (TNO, Institute of Applied Physics, Delft, The Netherlands). It was compiled to run on UNIX workstations.

The outline of the three-stage algorithm is as follows. In the first stage, the analyst draws borders around the nucleus in planes that cut approximately through the center of the nucleus under consideration. These planes are where the nuclear boundaries are generally sharpest and thus most visible. The borders serve as inputs to the second stage, which the algorithm uses to interpolate the entire surface of the nucleus and thus achieves segmentation. However, the interpolated surface cannot be expected to match exactly the true surface of the nucleus. Consequently, in an optional third stage, the algorithm automatically optimizes the interpolated surfaces based on edge strengths, which are measured as changes in the intensity of adjacent voxels in the original image. The results from the algorithm are not significantly affected by the relative size of voxels in the x, y, and z dimensions, and thus there is no requirement for the voxels to be isometric. Each stage of the algorithm is described in detail below, and the workflow and instructions for operating the algorithm are listed in the appendix.

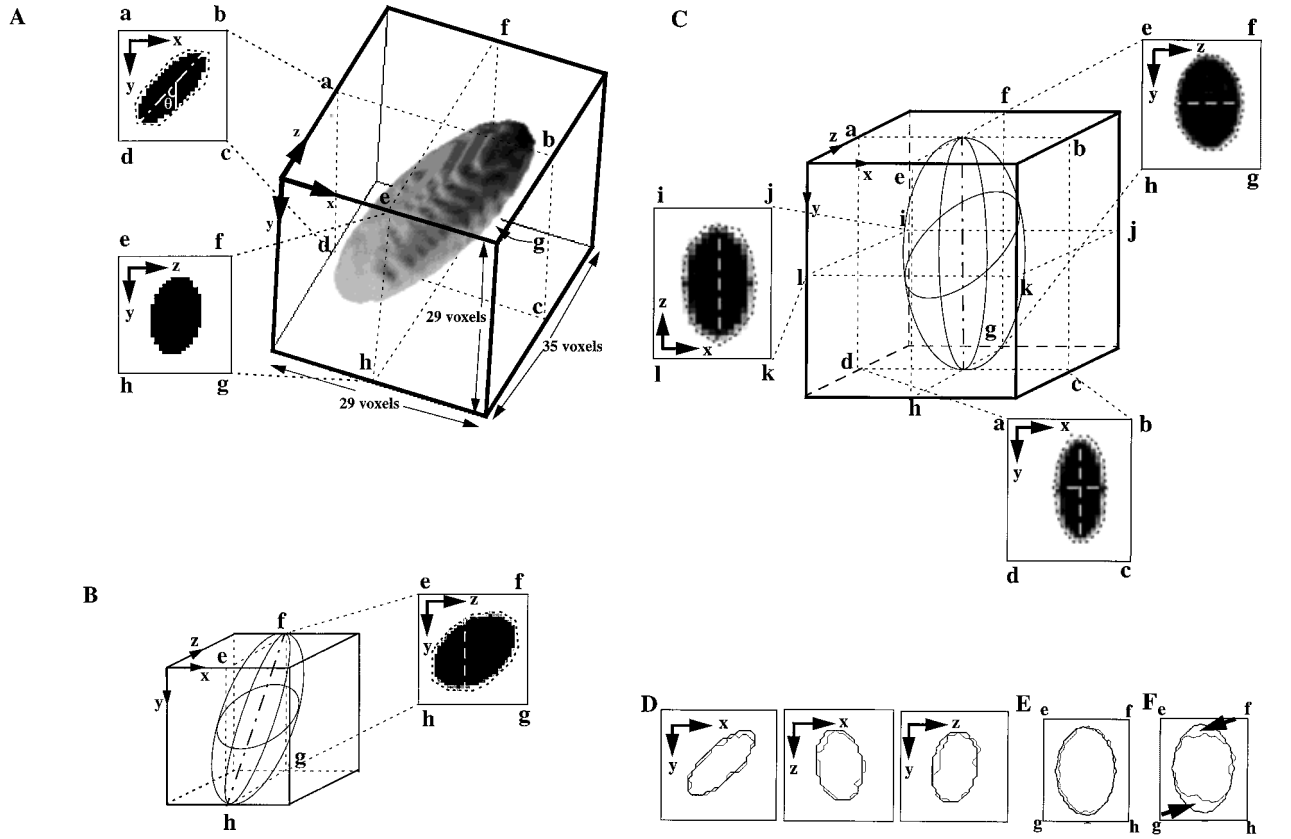

FIG. 1. Interactive segmentation of an ellipsoid. **A:** Right, ellipsoid of major axis: minor axis: minor axis = 3:2:1 and surface rendered using AVS (Advanced Visual Systems Inc., Waltham, MA). The major axis is approximately along the line joining the opposite corners of the 3D image. Planes abcd and efgh are, respectively, the xy and yz planes that cut approximately through the center of the ellipsoid. Such planes do not show the full extent of the object. The dotted line in abcd is the first border drawn by the analyst; the dash-dot line (white) is the principal axis calculated from this border, and θ is the angle of the principal axis with the y axis of the image. **B:** Left, the ellipsoid in A right after rotation by θ, so that the principal axis in abcd of A is parallel to the y axis. Plane efgh is the yz plane through the center of area (CoA) calculated from the first drawn border. This efgh plane is not the same as the one shown in A, which was before rotation. The vertical dashed line in efgh is the edge-on view of the first drawn border (dotted line in abcd of A). It is used to direct the analyst to the nucleus currently being segmented. The dotted line in the plane is the second border drawn by the analyst. **C:** Middle, the ellipsoid after the second rotation which makes the principal axis in ''efgh'' of B parallel to the y axis of the 3D image, and now makes the major axis of the ellipsoid (dash-dot line in outline of ellipsoid) parallel to the y axis of the 3D image. ''ijkl'' is the xz plane through the center of volume (CoV) of the object. The dashed line in this plane is the edge-on view of the second drawn border and the dotted line is the third drawn border. Planes efgh and abcd are, respectively, the yz and xy planes through the CoV of the object. They show the edge-on views of the previously drawn orthogonal borders (dashed lines) and borders drawn by the analyst (dotted lines). **D:** Result of segmentation (without optimization). The xy, xz, and yz planes through the CoV of the ellipsoid (A) show the true surface (thick lines) and interpolated surface (thin lines). **E:** Segmentation result (without optimization) in plane efgh of C. **F:** Segmentation result (without optimization) in plane efgh of C, which was generated by directly interpolating the three orthogonal borders around the ellipsoid shown by the thin lines in D and omitting the prior rotations from the orientation shown in A to that shown in C.

Stage 1: Drawing borders around the nucleus. The aim of this stage is to obtain three orthogonal, planar borders encompassing the full extent of the nucleus being segmented. This is accomplished by the analyst drawing five borders around the nucleus, the first two of which are used to estimate the orientation of the nucleus. We assume for the purposes of calculating the orientation that the nucleus can be modeled as an ellipsoid and thus define orientation as the angles the principal and minor axes of the ellipsoid make with the 3D image. Later we show by experiment that this model leads to accurate segmentation of nuclei that depart considerably from ellipsoids. Next, the nucleus is rotated so that its principal and minor axes are parallel to the x, y, and z axes of the 3D image. This rotation ensures that the next three borders, which are drawn around the rotated nucleus in orthogonal xy, xz, and yz image planes that cut approximately through the center of the nucleus, encompass the full extent of the nucleus. If these three borders do not encompass the full extent of the nucleus, then the segmented object that results from interpolation in stage 2 will represent only part of the nucleus. This error is significant for elongated nuclei whose principal and minor axes are not parallel to the x, y, or z axes and is illustrated in Figure 1A. Figure 1A shows an ellipsoid with its principal axis along the line joining the opposite corners of the 3D image. The xy (plane abcd in Fig. 1A), xz (not shown), and yz (efgh) image planes through the center do not show the full extent of the ellipsoid. However, after rotation of the ellipsoid so that its principal axis is parallel to the y axis

and minor axes are parallel to the x and z axes (Fig. 1C), the xy (abcd), xz (ijkl), and yz (efgh) planes do show the full extent of the ellipsoid and lead to accurate segmentation.

Figure 1D–F shows the segmentation results. Figure 1D shows xy, xz, and yz planes through the center of the ellipsoid in its original orientation (Fig. 1A), with the true and interpolated surface of the ellipsoid represented as thick and thin lines, respectively. The segmentation is considered to be accurate based on quantitative evaluation. Figure 1E shows the result again after rotating the ellipsoid and segmented object to the orientation shown in Fig. 1C. However, if the initial rotation of the ellipsoid was omitted and the three borders indicated by the thin lines in Figure 1D (they could have been drawn by the analyst) were used directly to interpolate the segmented object, the result in Figure 1F is obtained after rotating the ellipsoid and segmented object to the orientation shown in Figure 1C. It shows significant underestimation of the ellipsoid (arrows in Fig. 1F) because the borders in Figure 1D do not encompass the full extent of the ellipsoid.

The first action by the analyst is to select an xy plane from the original image that passes approximately through the center of the object being segmented (e.g., plane abcd in Fig. 1A) and to draw a border around it (dotted line in plane abcd). Next, the algorithm uses this border to calculate the center of area (CoA) of the (2D) shape defined by the border and the angle θ that the principal axis makes with the y axis. The angle of the principal axis is calculated by using the expression:

$$0.5 \times \arctan(2 \times \mu_{11}/(\mu_{20} - \mu_{02})),$$

where μ_{ij} are the second-order central moments of the shape (4).

Using the Affine transform (13), the algorithm then rotates the 3D image about the z axis through the CoA by θ, which results in the principal axis in plane abcd of Figure 1A becoming parallel to the y axis. Figure 1B shows the outline of the ellipsoid in Figure 1A after this rotation.

In the next step, the algorithm extracts from the 3D image of the rotated ellipsoid (Fig. 1B, left) the yz plane at the x position of the CoA calculated above (plane efgh in Fig. 1B) and displays it to the analyst with a vertical line (dashed line in plane efgh) showing the edge-on view of the first drawn border. This line serves to direct the analyst to the object being segmented. The analyst draws a border around the ellipsoid (dotted line in plane efgh). Then, the algorithm calculates from this border the CoA and the angle of the principal axis and then rotates the 3D image about the x axis through the CoA so that the principal axis is parallel to the y axis. After this second rotation, the ellipsoid is oriented so that its major axis is approximately parallel to the y axis of the 3D image (Fig. 1C, middle).

The algorithm uses the first and second borders drawn by the analyst to estimate the subvolume of the 3D image containing the nucleus under consideration. This enables further analysis to be speeded up by restricting it to this subvolume. In general, the subvolume is set in each dimension to twice the size of the nucleus as estimated from the first and second drawn borders.

Next, the algorithm rotates the ellipsoid so that its minor axes are parallel to the x and z axes of the image, which is necessary for obtaining orthogonal borders most likely to encompass the full extent of the ellipsoid. This is done as follows. The algorithm displays the xz plane through the CoA (plane ijkl in Fig. 1C) and the analyst draws a border around the ellipsoid (dotted line in plane ijkl). The algorithm calculates the CoA and the angle of the principal axis of the shape defined by this border and rotates the ellipsoid about the y axis through the CoA so the principal axis is parallel to the z axis. (In the example shown in Fig. 1C, the principal axis, dashed line in plane ijkl, was already approximately parallel to the z axis before rotation.) At this point, the ellipsoid has the best possible orientation with respect to the axes of the 3D image for drawing three orthogonal borders in xy, xz, and yz planes that encompass the full extent of the ellipsoid. The drawn border in plane ijkl serves as the first of the three orthogonal borders after rotation by the same amount as above.

In the final step, the analyst draws orthogonal borders in the yz and xy planes through the center of volume (CoV) of the object (planes efgh and abcd, respectively, in Fig. 1C).

Stage 2: Automatic interpolation of the surface from the three orthogonal borders. The design criteria for this stage were to have the interpolated surface exactly fit the three orthogonal borders produced in the first stage and be smooth between them. To meet these criteria, we employed an easily implemented geometrical construction. The planes outlined by the three orthogonal borders divide the object into eight octants, and interpolation is performed separately for each one. Figure 2A shows one of these octants, with the origin of the coordinate system shifted to the intersection point of the planes. To define the entire surface of the object in this octant, it is necessary to calculate a z coordinate for every (x, y) coordinate inside the plane region bounded by the x axis, y axis, and the border in the xy plane (shaded area in Fig. 2A). For example, for the point $(x_i,y_i,0)$ in the shaded area, we will use information from the three drawn borders to calculate z_i such that the point (x_i,y_i,z_i) lies on the surface of the nucleus. We accomplish this in two steps. First, we translate the border in the xz plane along the y axis to y_i (dashed line in Fig. 2B). Then, the translated border is linearly scaled in the x direction so that the end of the translated border, $(x_o,y_i,0)$ moves to $(x_i',y_i,0)$. The dash-dot curve in Figure 2B is the translated and scaled border, and the value of z at (x_i,y_i) on it, z_i^x, is an estimate of z_i based on only the drawn border in the xz plane and by ignoring the drawn border in the yz plane. This procedure of translation and scaling is repeated for all y coordinates in the shaded area. Next, the equivalent procedure is performed by using the drawn border in the zy plane to obtain a second estimate of z_i, z_i^y based on only the yz border but ignoring the xz border (Fig. 2C). Finally, we combine the two estimates of z_i: z_i^x and z_i^y by multiplying

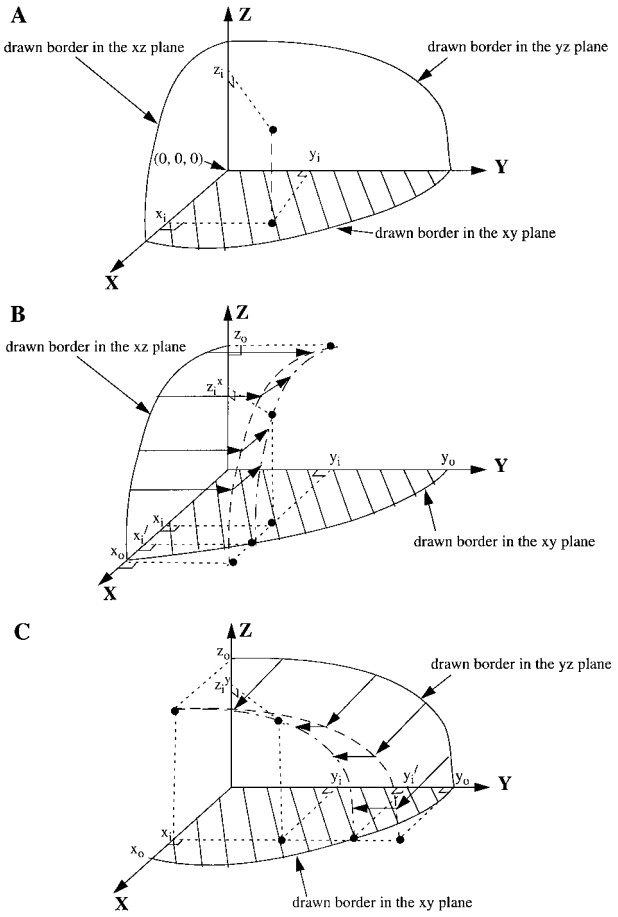

FIG. 2. Interpolating the surface from the three orthogonal drawn borders. **A:** An octant from a 3D image showing schematically segments of the three orthogonal drawn borders drawn around a nucleus; (x_i,y_i,z_i) is a point on the surface of the nucleus and will be estimated by stage 2 of the algorithm. **B:** The dashed line from $(0,y_i,z_0)$ to $(x_0,y_i, 0)$, is a translation in the y direction of the drawn border in the xz plane. The arrows parallel to the y axis indicate the translation that took place. The dash-dot line from $(0,y_i,z_0)$ to $(x'_i, y_i, 0)$ is the dashed line after linear scaling in the x direction, so that $z = 0$ at the intersection of the dash-dot line and the xy border, $(x'_i, y_i, 0)$. The arrows parallel to the x axis indicate the scaling. **C:** The dashed line from $(x_i,0,z_0)$ to $(x_i,y_0,0)$ is a translation in the x direction of the drawn border in the yz plane. The dash-dot line from $(x_i,0,z_0)$ to $(x_i,y'_i, 0)$ is the dashed line after scaling, so that $z = 0$ at the intersection of the dash-dot line and the xy border, $(x_i,y'_i, 0)$.

them together and dividing the result by z_o. The result is a smooth, interpolated surface over the entire octant that exactly matches the drawn borders. Mathematically, the interpolation procedure is given by the equation

$$z_i = Z^x(x_i'') \times Z^y(y_i'')/z_o,$$

where $Z^x(x)$ is the value of z on the xz drawn border at x, $Z^y(y)$ is the value of z on the yz border at y, $x_i'' = x_i \times x_o/x'_i$ and $y_i'' = y_i \times y_o/y'_i$. The value x_i, y_i, z_i, x_o, y_o, z_o, x'_i and y'_i are defined in Figure 2.

Stage 3: Automatic optimization of the interpolated surface. It is expected that the interpolated surface of the nucleus will not be exact because stages 1 and 2 contain the following approximations: the orthogonal borders from stage 1 may not be drawn exactly over the true borders; they may not encompass the full extent of the nucleus because of imperfect orientation or irregularity of the shape of the nucleus; and the interpolation algorithm cannot account for properties of the nuclear surface that are not evident from the orthogonal borders. Thus, we developed an automatic surface optimization algorithm that moves the interpolated surface toward the true surface as indicated by edge information in the original image. It is based in a 2D version (20) and is a variation of gray-level thinning (31). The algorithm was designed to behave robustly in the presence of uncertainties (e.g., noise) by letting uncertainties stop the optimization prematurely. This introduced the possibility that the resulting surface was intermediate between the interpolated and true surfaces but prevented the resulting surface from deviating significantly from the true surface.

In the first step, the algorithm measures the likelihood that each voxel is on the surface. Because the segmentation procedure is intended for images of internally stained nuclei, where large changes in image intensity exist at the surface of nuclei, the magnitude of these intensity changes (edge strengths) at each voxel in the original image are used as an indication of this likelihood. The edge strengths are taken as the magnitude of the response from a derivative Gaussian filter with a standard deviation of 1.5 voxels applied in the x, y, and z directions to the image.

In the second step, optimization takes place by removing voxels from the surface if such action increases the average edge strength over the surface of the nucleus. Average edge strength is defined as the sum of the edge strengths of the voxels on the surface divided by the number of these voxels. The algorithm performs this task by successively visiting each of these voxels. For each one, the average edge strength of the surface within the $3 \times 3 \times 3$ voxel volume surrounding the voxel under consideration is calculated. Next, the voxel under consideration is temporarily removed, the new surface voxels in the $3 \times 3 \times 3$ volume is identified, and the average edge strength of the new surface within the $3 \times 3 \times 3$ volume is calculated. If the average edge strength of the new surface is greater than that of the old surface, the voxel is permanently removed. If after visiting every voxel on the initial surface at least one voxel was removed, then the algorithm repeats.

In the third step, optimization takes place in an analogous way, except that voxels are added to rather than removed from the surface. Removal of voxels is performed first because analysts usually draw borders slightly outside the nucleus, leading to an interpolated surface slightly larger than the nucleus.

After optimization, the analyst decides whether to keep the optimized surface or revert to the interpolated one from stage 2. Optimization may not be desirable when segmenting extremely low contrast and noisy images in which false edges, from artifacts outside and inside the nuclei but close to the nuclear surface, may be stronger than the edge strengths of the surface. In this situation,

optimization is at risk of moving the interpolated surface toward the false edges and further away from the correct surface. Another example when optimization is not desirable is in DNA ploidy measurements, which require measuring the integrated fluorescence signal from individual nuclei. Because of the PSF of the microscope, some of the signal is recorded in voxels that are outside the nucleus. In this situation, the most accurate measurements are obtained by using segmented objects that are deliberately too large rather than using objects whose surface accurately match those of the nuclei (19).

Preparation of Computer-Generated Test Objects

To test the performance of the segmentation procedure, artificial 3D solid, gray-valued objects that had similar sizes and shapes to nuclei of thick tissue sections imaged by confocal microscopy were generated.

The first two objects were spheres with diameters of 20 and 50 voxels. For an actual nucleus of diameter 7.5 μm, they would correspond to voxel sizes of 0.375 and 0.15 μm, respectively. These were similar to the voxel size of the 3D images of tissue specimens used in this study. The third object was the ellipsoid shown in Figure 1A, which had a major axis of 30 voxels. These three objects are regular ellipsoids and the algorithm will by design correctly orient the objects in the image (stage 1) and accurately interpolate the surfaces (stage 2). However, the algorithm is not explicitly designed to produce a correct segmentation for less regular objects; therefore, it was tested with such objects. The fourth and fifth objects were a curved ellipsoid and curved disc, respectively, and were designed to represent the shape of a nucleus when another nucleus appeared to push into it. The curved ellipsoid was generated from a straight ellipsoid of major axis of 30 voxels and minor axes of 10 voxels. It was bent so that the major axis became a quarter circle, resulting in a shape similar to a fat banana. It was then oriented so that the line joining the ends of the major axis was along the opposite corners of a cubical 3D image. The curved disc was generated from a straight ellipsoid with the major axis and one of the minor axes, both equaling 30 voxels, and the other minor axis equaling 10 voxels. It was bent so that the major axis became a quarter circle and then bent again so that the long minor axis also formed a quarter circle. The direction of the second bend was such that the ends of the major axis and long minor axis lay in a plane. It had the appearance of a satellite dish. The combination of the two bends introduced a concavity on the side of the disc facing the common center of the two quarter circles. The concavity is visible in Figure 3. The object was oriented so that the ends of the major axis were approximately along the z axis and the ends of the long minor axis were approximately along a diagonal line at 450° in the xy plane. The sixth object was a dumbbell generated from two spheres of diameter 20 voxels, which were superimposed so that the line joining their centers was 12 voxels long and parallel to the z axis. The object was then rotated 20° about the y axis. This object could represent either a single bipolar nucleus or two touching, partially spherical nuclei such that the interface between them was a flat circular surface.

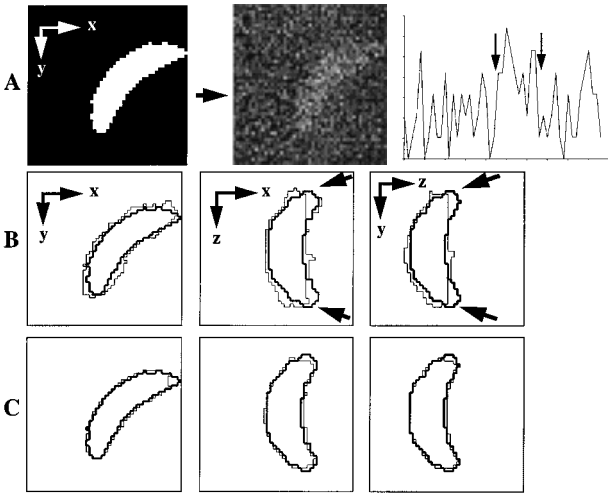

FIG. 3. Interactive segmentation of the curved disk. **A:** An xy plane through the center of the curved disk, without noise (left) and with Poisson noise added such that the SNR is 1.0 (middle). On the right is a line profile across the middle image at the position indicated by the horizontal arrow. The two vertical arrows indicate the edges of the curved disk. **B:** Results of interactive segmentation (without optimization) on the curved disk. The xy, xz, and yz planes pass through the center of the disk in the original image and show the true surface (thick lines) and interpolated surface (thin lines). Arrows indicate regions at the ends of the curved disk where large deviations between the true and interpolated surface exist. **C:** Results after optimization of the interpolated surface.

Acquisition, Preparation, Staining, and Imaging of Tissue Specimens

Skin specimens were obtained from the archives of the Dermatopathology Section of the Departments of Pathology and Dermatology (UCSF) and a breast cancer specimen was obtained from the Department of Pathology (California Pacific Medical Center, San Francisco). All specimens had been fixed in 10% neutral buffered formalin and processed with standard histological paraffin-embedding techniques. They were cut into 20-μm-thick sections and stained with propidium iodide (PI) at 0.1 μg/ml to label the nuclei internally (37). The centromeric regions of chromosome 1 were also stained by using fluorescence ISH (FISH) (37), but analysis of FISH signals is not part of the present study. The skin specimens were imaged with an MRC-1000 confocal imaging system (Bio-Rad Microscience Ltd., Hemel Hempstead, England) equipped with a Diaphot 200 microscope (Nikon Inc., Instrument Group, Garden City, NY), a 60×, 1.4 NA planapo objective lens (Nikon), and an Argon/Krypton (Ar/Kr) laser. The fluorescein-labeled probe and the PI were imaged simultaneously by using the 488- and 568-nm laser lines and collecting the emission light between 522 and 535 nm (fluorescein signal) with one photo multiplier tube (PMT) and light longer than 585 nm (PI signal) with another PMT. The breast specimen was imaged with a laser scanning microscope 410 (Carl Zeiss Inc., Thornwood, NY) equipped with an Axiovert 100 microscope (Zeiss), a 63X, 1.4 NA

Table 1
Accuracy of the Algorithm When Applied to Computer-Generated Objects

Object	Average distance between segmented and true surface (in voxels)	Percentage of voxels on the segmented surface that are d voxels from the true surface					
		$d = 0$	$0 < d \leq 1$	$1 < d \leq 2$	$2 < d \leq 3$	$3 < d \leq 4$	$4 < d \leq 5$
Sphere (diameter = 20 voxels)	0.59	45	47	7.8	0	0	0
Sphere (diameter = 50 voxels)	0.85	28	50	19	1.8	0	0
Ellipsoid (Fig. 1)	0.54	50	43	6.5	0.4	0	0
Curved ellipsoid	0.69	38	51	11	0.7	0	0
Curved disc	0.86	33	44	18	4.2	0.9	0.3
Dumbbell as one object	0.78	35	45	18	1.8	0	0
One of the partial spheres in the dumbbell (Fig. 4)	0.57	47	47	5.9	0.3	0	0

plan-apochromat objective lens (Zeiss), and an Ar/Kr laser. The fluorescein-labeled probe and the PI were imaged sequentially. First, the fluorescein label was imaged by using the 488-nm laser line and collecting emissions between 515 and 565 nm; then, the PI was imaged by using the 568 nm laser line and collecting emissions longer than 590 nm. On both confocal microscopes, a series of 2D optical sections, 0.5 μm apart, were acquired starting above the top surface of the section and extending below the bottom surface. A zoom of factor 2.0 was used during the scanning, resulting in a voxel size of 0.18 μm in the x and y dimensions for the skin specimens and of 0.2 μm for the breast specimen. Each optical section from the skin specimens was the average of three successive scans. Images were transferred to a UNIX workstation for archiving and analysis.

Algorithm Evaluation Using the Computer-Generated Objects

The computer-generated objects were segmented with and without optimization. The sixth object was segmented under two assumptions of what the object actually represents, first as a single dumbbell and second as two touching partial spheres. The segmentation results were assessed visually and objectively. Objective assessment consisted of counting the number of voxels in the true object that were not in the segmented object (false negatives, FN), and number of voxels in the segmented object that were not in the true object (false positives, FP). For all objects, it was observed that without optimization FP was much larger than FN, which was consistent with the analyst drawing slightly outside the objects. Therefore a single, 6-connected 3D binary erosion was applied to the segmented objects. This application made FN > FP for some objects and FP > FN for others. Next, for each object, the distance of each voxel on the surface of the segmented object to its closest voxel on the surface of the true object was calculated. This calculation was implemented by using the Euclidean distance transform (26) to calculate the distance from every voxel in the 3D image to the closest voxel on the surface of the true object. These distances were assigned to each voxel on the surface of the segmented object. They were used to calculate the average distance of the segmented surface from the true surface and the distribution of distances over the segmented surface voxels for each object (i.e., the proportion of segmented surface voxels on the true surface, where distance = 0, the proportion between 0 and 1 voxels from the true surface, the proportion between 1 and 2 voxels, etc.)

The results from this analysis were poorest for the 50 voxel diameter sphere and the curved disc (Table 1); therefore, these objects were used further to assess the optimization stage, the effects of noise, and analyst variability. These two objects were segmented twice more to assess analyst variability. Next, noise was added to the images of these objects. The SNR was defined as

$$\mathrm{SNR} = (m_o - m_b)/(\sigma_o^2 + \sigma_b^2)^{0.5},$$

where m_o is the mean intensity inside the object, m_b is the mean intensity in the background of the image, σ_o is the standard deviation of the intensities inside the object, and σ_b is the standard deviation of the intensities of the background. Noise was added at levels to make the SNR 0.5 for the sphere image and 1.0 for the curved disc image. These were the lowest SNRs in which the objects remained visible (Fig. 3A, middle). Four types of noise were added to each image: Gaussian, Poisson, uniform and binary, and each image was segmented once for each type of noise with and without optimization.

Algorithm Evaluation Using Tissue Specimens

The 3D images of the tissue specimens were segmented directly without any preprocessing such as interpolation to create isometric voxels. They were segmented with and without the optimization stage. Assessment of the results was done by visual examination because not knowing the true surfaces of the nuclei precluded the use of more objective assessment.

RESULTS

Computer-Generated Objects

Table 1 shows the average distances between the segmented surfaces before optimization and the true surfaces and the distribution of the distances between the segmented and true surfaces for the noise-free computer-generated objects for the first time these objects were segmented. The average distances are generally less than 1

Table 2
Accuracy of the Algorithm With and Without Optimization When Applied to Computer-Generated Objects With and Without Noise[a]

Object	No noise, no optimization	No noise, with optimization	With noise, no optimization	With noise, with optimization
Sphere (diameter = 50 voxels)	0.75 ± 0.13	0.23 ± 0.02	1.11 ± 0.39	0.33 ± 0.01
n	3	3	4	4
Curved disc (Fig. 3)	0.96 ± 0.11	0.42 ± 0.03	0.96 ± 0.19	0.46 ± 0.02
n	3	3	4	4

[a]Results are expressed as the mean ± sample standard deviation of the average distances between the segmented and true surfaces in voxels. n, number of segmentations performed. For the noisy images (columns 3 and 4), the results from the four different types of noise are combined.

voxel, although at certain places the distances from the segmented to the true surfaces were more than 1 voxel. Figure 1D shows the true and segmented surfaces for the ellipsoid (which had the lowest average distance) in xy, xz, and yz planes that pass through its center. The results were poorest for the 50-voxel-diameter sphere and the curved disc; therefore, these objects were used further to assess the optimization, the effect of noise, and analyst variability. The results (Table 2) show that optimization significantly improves the accuracy of the final surface (compare column 1 with 2 and column 3 with 4). After optimization, the average distances were all less than 0.5 voxel, even in the presence of high noise. This result corresponds to an error of less than 10% when estimating the volume of the objects. Figure 3A shows the curved disk before noise was added (left), after addition of Poisson noise (middle), and a line profile through the noisy image at the horizontal arrow. The vertical arrows in the line profile show the edges of the curved disk. Figure 3B shows the true surface of the curved disk overlaid with the segmented surface before optimization from using the image with Poisson noise added (Fig. 3A, middle). Note that the interpolated surface was able to capture the concavity of this object (Fig. 3B, left). The reason for the large deviation at the ends of the disk in the xz and yz planes (arrows in Fig. 3B) is from difficulties in visualization of the object, leading to drawn borders that did not accurately encompass the object. Optimization was largely able to correct for these deviations (Fig. 3C), as it can for other types of irregularities (protrusions and indentations) on the surface of objects (results not shown). The small standard deviations relative to the means in columns 1 and 3 of Table 2 show that analyst variability was not a major source of error. Furthermore, these standard deviations drop to very low values after optimization (columns 2 and 4 of Table 2) because of the robustness of the optimization algorithm. Overall, the accuracy of the segmentation procedure using optimization was considered adequate for many applications.

Three types of error exist in stages 1 and 2 of the segmentation procedure: first, the analyst is imprecise in drawing borders; second, the method of measuring the orientation of the object and rotating it does not always result in three orthogonal borders encompassing the full extent of the object, thus leading to a segmented object smaller that the true object; and third, the interpolation algorithm cannot precisely determine the entire surface from the borders. All three errors are dependent on the complexity of the true shape of the object.

The first error occurs because of the analyst's imprecision when drawing borders. This error increases in an absolute sense with the size of the objects because the displays used for drawing borders contain more and smaller surface voxels for the larger objects. This error is observed when comparing the results for the two spheres listed in Table 1. The average distance between the segmented and true surfaces of the 20-voxel-diameter sphere (0.59) is less than that of the 50-voxel-diameter sphere (0.85). However, the average distance relative to the radius of the sphere is 0.017 for the large sphere, which is smaller than the relative average distance for the small sphere of 0.030. The other two types of errors for the two spheres would be expected to behave similarly.

The second error occurs because on occasions the three borders drawn after rotation of the object do not encompass the full extent of the object. This is caused by suboptimal determination of the orientation of the object and becomes worse as the objects become less regular in shape. This is indicated in Table 1 by the greater average distances for the curved ellipsoid, curved disk, and dumbbell as one object (distances from 0.69 to 0.86) versus the more regular objects of similar volume, i.e., the 20-voxel-diameter sphere, ellipsoid, and one partial sphere of the dumbbell (distances from 0.54 to 0.59). The curved disk also had the greatest proportion of surface voxels two or more voxels from the true surface (5.4%) in part because of this error.

Errors from the third source occur because the interpolation algorithm (stage 2) cannot account for properties of the surface that are not evident from the orthogonal borders. This error increases for increasingly irregular nuclei, but it also exists for regular nuclei. For example, even if the orthogonal borders were drawn perfectly around the full extent of the ellipsoid shown in Figure 1, the interpolation algorithm would still not give an exact result because it does not explicitly fit an ellipsoid between the borders. The error in this case would be an underestimate of its size, equaling an average distance between the segmented and true surfaces of 0.1 voxel. Also, the interpolation algorithm will generally produce slightly different results if the z axis is interchanged with the x or y axis.

The optimization algorithm does not produce perfect results even for the noise-free images for two reasons. First, the surface of the object is defined as the set of object voxels adjacent to background voxels, but the edge strengths of background voxels (based on our definition of edge strength) adjacent to the object can be as high or higher than the edge strengths of the adjacent surface voxels, depending on the shape of the object. Consequently, the optimization algorithm will in places incorrectly move the surface out by 1 voxel to the adjacent background voxel. The other source of imperfect results after optimization is when the nonoptimized surface deviates by a large distance from the true surface. In this situation, continuously increasing edge strengths may not exist everywhere between the nonoptimized surface and the true surface, thus causing the optimization to stop prematurely. This error partly explains the poorer results for the curved disk compared with the 50-voxel sphere (column 4 of Table 2) because of the large deviation between the interpolated and true surfaces at the ends (Fig. 3B). Noise in the images increases the error after optimization (column 4 vs. column 2 in Table 2) because noise creates additional voxels with high edge strengths.

One of the attributes of our segmentation algorithm is that the analyst draws in orthogonal planes that cut approximately through the center of the object, which are the most suitable planes for visualizing the overall shape of the object and for discerning its surfaces. The effectiveness of this approach is illustrated by the segmentation of the dumbbell, where the axis between the centers of the two partial spheres comprising this object makes an angle of 20° with the z axis. Figure 4A shows the set of consecutive xy planes (analogous to a standard confocal z series of images) through the central region of the dumbbell, where both partial spheres are present. It is essentially impossible to see that this object may be made up of two partial spheres from these planes; the only hint is a pair of opposing indentations in the middle plane (arrows in the middle image of Fig. 4A). Thus, it would be very difficult to segment them by the conventional method of drawing around them in each xy plane. However, in the method we describe, which displays the object from different directions, the neck between the two spheres is clearly recognized. Figure 4B shows the resulting segmentation of one of the partial spheres in the same xy planes as shown in Figure 4A. The last plane appears to show significant deviation between the segmented and true surfaces. However, the distance between the true and interpolated surfaces is actually not more than 1 voxel in the direction perpendicular to the plane of this plane.

Tissue Specimens

Figure 5A,B shows xy planes through a 3D image of the epidermal layer of normal skin overlaid with the segmented surfaces of the nuclei before and after optimization, respectively. The surfaces before optimization are slightly larger than the nuclei, reflecting the tendency of the analyst to draw slightly outside the nucleus, but after optimization the segmented surfaces closely match the

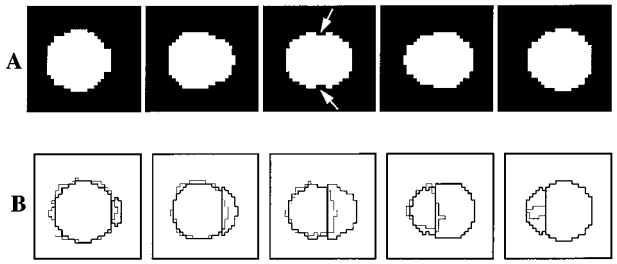

FIG. 4. Interactive segmentation of the dumbbell. **A:** Set of five consecutive xy planes through the central part of the dumbbell where both partial spheres forming the dumbbell are present. The arrows in the middle plane indicate the interface between the two partial spheres. **B:** Results of the interactive segmentation (without optimization) showing the true surfaces of the two partial spheres forming the object (thick lines) and the interpolated surface for the left object (thin line).

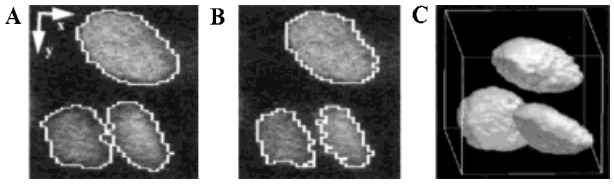

FIG. 5. Interactive segmentation of a 3D image of normal skin. **A,B:** The xy plane from the original 3D image overlaid with the nuclear borders determined by the segmentation procedure before (A) and after (B) optimization. **C:** Wire frame surface rendering of the three segmented nuclei before optimization.

surfaces of the nuclei as judged by visual examination. Figure 5C is a surface rendering (AVS) of the three segmented nuclei before optimization.

Figure 6 shows the results of segmenting a 3D image of a histologically normal region of the tissue section from the breast cancer specimen. The left column shows xy and xz plane pairs through the approximate center of the first three (of a total of 29) segmented nuclei. The middle column is the same image overlaid with the surfaces before optimization. The arrows and arrowheads indicate examples of background inside the segmented regions and parts of nuclei outside the segmented regions, respectively. These imprecisions in the position of the surfaces were corrected by optimization, producing the surfaces shown in the right column. Similar results were obtained for the other 26 nuclei.

The segmentation method was applied to an image of a malignant melanoma specimen that was deliberately selected because of its low contrast, high noise, and high clustering of nuclei. These features are indicated in the line profile in Figure 7E and made segmentation by drawing the border of each nucleus in successive xy planes impossible. Figure 7A–D shows xy and xz planes from the 3D image overlaid with the interpolated surfaces. For this image, we did not expect optimization to improve the result over the interpolated one. We also hypothesize that no automatic method could segment these nuclei.

DISCUSSION

In the present study, we developed an interactive algorithm for segmenting objects in 3D images and illus-

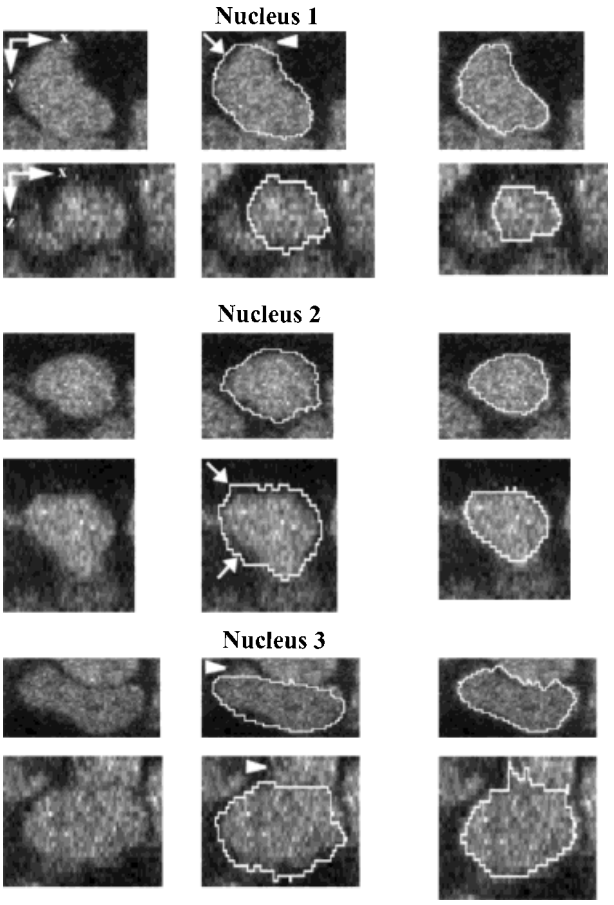

FIG. 6. Interactive segmentation of a 3D image from the breast cancer specimen. The left column is xy and xz image planes through the approximate center of three nuclei. The middle column is the same images overlaid with the interpolated surfaces of the nuclei from stage 2 of the algorithm. The arrows and arrowheads show examples of background inside and parts of nuclei outside the segmented regions, respectively. The right column shows the images overlaid with the surface after optimization in stage 3 of the algorithm.

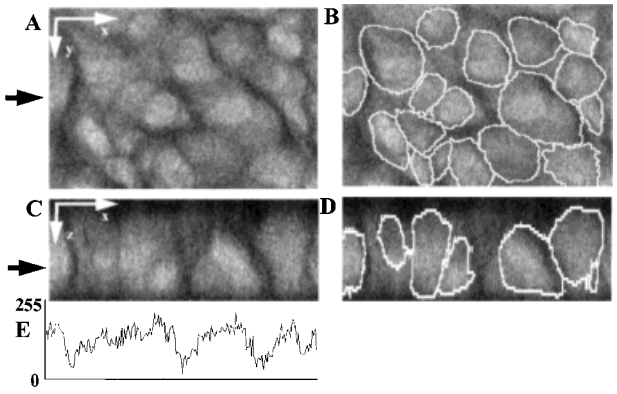

FIG. 7. Interactive segmentation of a 3D image of melanoma. **A–D:** The xy (A and B) and xz (C and D) planes overlaid with the interpolated surfaces (before optimization). The arrow in A indicates the position of the xz plane and the intensity profile (E). The arrow in C indicates the position of the xy plane and the intensity profile. **E:** Intensity profile at the position of the arrows in A and C.

trate its application to confocal images of nuclei inside thick tissue sections. It was developed to provide a way to segment all nuclei within intact tissue sections of cancer specimens. Its application will be in cancer biology studies in which individual nuclei must be analyzed within the context of their environment and to provide a means to verify the performance of automatic segmentation algorithms that are now under development. Our approach has important advantages over the standard interactive method of drawing around the nucleus in each successive xy plane because one draws only five borders per nucleus and in planes that cut approximately through the center of the nucleus where borders are most visible. The remainder of the surface of the object is filled by using interpolation. Our method is reasonably accurate, even for nonellipsoidal objects, but extensions of the algorithm to improve its speed and accuracy for less regular objects could be conceived. Speed could be increased by adopting the semiautomatic contour extraction method of Wu and Barra (39). This method requires the analyst to specify four contour points in a 2D plane, from which the complete border in the plane is interpolated. Accuracy could also be increased by using the drawn borders to predict the regularity of the shape of the nucleus and then require, if necessary, that the analyst draws additional borders around the object. However, this would increase the amount of interaction by the analyst and thus reduce the advantage of our method over drawing around the object in every successive plane. Instead, we chose to provide an optimization algorithm that adjusted the interpolated surface to reflect the true surface more accurately.

The accuracy of the method was assessed by using computer-generated objects, and its capabilities and limitations were demonstrated on confocal 3D images of tissue (Figs. 5–7). Normal skin nuclei were sufficiently regular and convex in shape to be well segmented by the first two stages of our method, as was found also by Wu and Barra for interactive segmentation of 2D images (39). For the same reasons, the optimization stage resulted in very accurate segmentation of these nuclei based on visual judgment. Similarly, accurate results were obtained when segmenting a breast cancer image. However, in this case, optimization was necessary to correct for inaccuracies in the interpolated surfaces caused by the more irregularly shaped nuclei. Application to a low contrast, noisy image of malignant melamona containing highly clustered nuclei showed that our interactive segmentation was still successful when other existing methods would be expected to fail. However, the accuracy of the segmentation in this images was particularly difficult to determine because the poor quality made visual interpretation uncertain. Nevertheless, we are confident that each segmented object corresponds to an individual nucleus.

Ongoing development efforts can be expected in due course to lead to automatic algorithms that correctly segment a greater proportion of nuclei from 3D images. Some of these improvements can be foreseen by the extension of 2D nuclear segmentation algorithms to 3D

and the adoption of algorithms for other applications, particularly those used in medical image analysis. Promising 2D automatic algorithms include those by Lockett and Herman (18) who used the gray-weighted distance transform (30) to combine image intensity information and a priori morphological information about nuclei in a way that was insensitive to noise and signal variations inside the nuclei. When tested on clustered nuclei (those nuclei not correctly segmented by only intensity thresholding of the image), more than 90% were correctly segmented in images of 2-μm breast and prostate sections. Similar results were obtained by Malpica et al. (23) on peripheral blood and bone marrow preparations. They used the morphological gray-scale reconstruction method of Vincent (38) to separate clustered nuclei. Dow et al. (9), by using a method that combined intensity information of the original image and shape information in the form of the distance transform, correctly segmented more than 85% of nuclei in 6-μm human melanoma sections. Their method is in concept similar to deformable boundary and surface methods that are currently being developed for segmentation of medical images (5). Many other promising automatic algorithms have been published, for example, the Hough transform (16), region growing (2,35,40), and morphology (24,36) based techniques. However, their practical utility is less predictable because their evaluation using sufficient numbers of nuclei has not yet been reported.

The medical imaging field offers a number of promising algorithms that could be applied to nuclear segmentation. Some of these algorithms seek to optimize the surface of the object by balancing edge/region parameters measured from the image with a priori information about the shape of the object (5,6,22,25). Others use a multiscale representation in which coarse scale information is used to obtain partial results that are used to guide the final segmentation obtained when using the fine scale information (10,28). These approaches, however, do not address in a direct way the problem of defining the surface between two different but clustered objects. However, they could offer improvements over our current optimization stage. Another improved optimization method may be the dynamic programming approach of Starink and Gerbrands for finding the globally optimal surface starting from an approximate surface (32). At present, many of these algorithms are too slow for segmenting large numbers (hundreds) of objects in an image.

Practical applications of the algorithm we present are envisioned for studies that require measurements on individual cells within the context of their environment. The necessary segmentation accuracy depends on the particular measurements. For example, if one is studying tissue architecture, as was done by Bigras et al. (3) to classify neuroendocrine tumors, then what is of primary importance in terms of segmentation is a one-to-one correspondence between the segmented objects and individual nuclei rather than accurate delineation of the surface of each nucleus. Our method would be 100% correct for this task as judged by visual examination of our images. An application where more accurate segmentation would be necessary would be studies measuring the volume of small groups of diseased cells in premalignant lesions. By keeping the tissue intact, small aberrant groups can be identified, but many would be lost by other techniques, such as flow cytometry (12). In such a study done by Irinopoulos et al. (12) on prostate lesions, significant differences were detected in the mean nuclear volume of nuclei in hyperplastic regions versus prostatic intraepithelial neoplasia (PIN), well-differentiated carcinoma and poorly differentiated carcinoma, and PIN regions versus well-differentiated carcinoma. These differences were observed when the coefficient of variation for the mean volume within each of the disease stages was 18% or greater. Because our method can measure nuclear volumes to less than 10% error, we would also be able to do this study. In conjunction with stoichiometric DNA staining and quantitative image acquisition, our method could be used for measuring the DNA content of individual nuclei in tissue sections (7,12,29). Similarly, in conjunction with techniques for automatically (27) or interactively (17) detecting punctate FISH signals, our method could be used for enumerating FISH signals per nucleus and for measuring the spatial positions of them within each nucleus (8,11,14).

LITERATURE CITED

1. Ancin H, Roysam B, Dufresne TE, Chestnut MM, Ridder GM, Szarowski DH, Turner JN: Advances in automated 3-D image analysis of cell populations imaged by confocal microscopy. Cytometry 25:221–234, 1996.
2. Belhomme P, Elmoataz A, Herlin P, Bloyet D: Generalized region growing operator with optimal scanning: Application to segmentation of breast cancer images. J Microsc 186:41–50, 1996.
3. Bigras G, Marcelpoil R, Brambilla E, Brugal G: Cellular sociology applied to neuroendocrine tumors of the lung: Quantitative model of neoplastic architecture. Cytometry 24:74–82, 1996.
4. Castleman KR: Digital Image Processing. Prentice-Hall, Englewood Cliffs, 1996.
5. Chakraborty A, Staib LH, Duncan JS: Deformable boundary finding in medical images by integrating gradient and region information. IEEE Trans Med Imaging 15:859–870, 1996.
6. Chang MM, Sezan MI, Tekalp AM, Berg MJ: Bayesian segmentation of multislice brain magnetic resonance imaging using three-dimensional Gibbsian priors. Opt Engin 35:3206–3221, 1996.
7. Czader M, Liljeborg A, Auer G, Porwit A: Confocal 3-dimensional DNA image cytometry in thick tissue sections. Cytometry 25:246–253, 1996.
8. Dietzel S, Weillandt E, Eils R, Münkel C, Cremer C, Cremer T: Three-dimensional distribution of centromeric or paracentromeric heterochromatin of chromosome 1, 7, 15 and 17 in human lymphocyte nuclei studied with light microscopic axial tomography. Bioimaging 3:121–133, 1995.
9. Dow AI, Shafer SA, Kirkwood JM, Mascari RA, Waggoner AS: Automatic multiparameter fluorescence imaging for determining lymphocyte phenotype and activation status in melanoma tissue sections. Cytometry 25:71–81, 1996.
10. Fritsch D, Pizer S, Yu L, Johnson V, Chaney E: Segmentation of medical image objects using deformable shape loci. Proc Info Proc in Med Imaging. 15th Int Conf IPMI, Berlin, 1997, pp 127–140.
11. Höfers C, Baumann P, Hummer G, Jovin TM, Arndt-Jovin DJ: The localization of chromosome domains in human interphase nuclei. Three-dimensional distance determinations of fluorescence *in situ* hybridization signals from confocal laser scanning microscopy. Bioimaging 1:96–106, 1993.
12. Irinopoulos T, Vassy J, Beil M, Nicolopoulou P, Encaoua D, Rigaut JP: Three-dimensional DNA image cytometry by confocal scanning laser microscopy in thick tissue blocks of prostatic lesions. Cytometry 27:99–105, 1997.
13. Jain AK: Fundamentals of Digital Image Processing. Prentice-Hall, Englewood Cliffs, 1989.

14. Léger I, Guillaud M, Krief B, Brugal G: Interactive computer-assisted analysis of chromosome 1 colocalization with nucleoli. Cytometry 16:313–323, 1994.
15. Lelievre S, Weaver VM, Bissell MJ: Extracellular matrix signaling from the cellular membrane skeleton to the nuclear skeleton: A model of gene regulation. Rec Prog Horm Res 51:417–432, 1996.
16. Lockett SJ, Rodriguez EG, Ortiz de Solózano C, Sudar D, Pinkel D, Gray JW: Automatic hough transform-based 3D segmentation of cell nuclei in thick tissue sections. Proc Microsc Microanal 3:1121–1122, 1997.
17. Lockett SJ, Thompson C, Sudar D, Mullikin J, Hyun B, Khavari R, Pinkel D, Gray J: Interactive algorithms for rapid chromosome copy number enumeration of individual whole cell nuclei inside intact tissue specimens. Proc SPIE 2412:43–49, 1995.
18. Lockett SJ, Herman B: Automatic detection of clustered, fluorescent-stained nuclei by digital image-based cytometry. Cytometry 17:1–12, 1994.
19. Lockett SJ, Jacobson K, Herman B: Quantitative precision of an automated, fluorescence-based image cytometer. Analyt Quant Cytol Histol 14:187–202, 1992.
20. Lockett SJ, O'Rand M, Rinehart CA, Kaufman DG, Herman B, Jacobson K: Automated fluorescence image cytometry: DNA quantification and detection of chlamydial infections. Analyt Quant Cytol Histol 13:27–44, 1991.
21. Mackin RW, Roysam B, Turner JN: Adaptive 3-D segmentation algorithms for microscope images using local in-focus, and contrast features: Applications to Pap smears. Proc Int Image Proc, Washington DC, 1995, pp. 23–25.
22. Malladi R, Kimmel R, Adalsteinsson D, Sapiro G, Casselles V, Sethian JA: A geometric approach to segmentation and analysis of 3D medical images. Proceeding of the Workshop on Mathematical Methods in Biomedical Image Analysis. IEEE Computer Society, Los Alamitos, 1996, pp 244–252.
23. Malpica N, Ortiz de Solózano C, Vaquero JJ, Santos A, Vallcorba I, García-Sagredo JM, del Pozo F: Applying watershed algorithms to the segmentation of clustered nuclei. Cytometry 28:289–297, 1997.
24. Marroquin EM, Santamaría E, Jové X, Socoró JC: Morphological analysis of mammary biopsy images. Proceedings of the 8th Mediterranean Electrotechnical Conference on Industrial Applications in Power Systems. Computer Science and Telecommunications, Bari, Italy, 1996, 2:1067–1070.
25. McInerney T, Terzopoulos D: Medical image segmentation using topologically adaptable surfaces. Proceedings of the 1st Joint Conference, Computer Vision, Virtual Reality and Robotics in Medicine and Medical Robotics and Computer-Assisted Surgery. Berlin, 1997, pp 23–32.
26. Mullikin JC: The vector distance transform in two and three dimensions. CVGIP: Graph Models Image Process 54:526–535, 1992.
27. Netten H, Young IT, van Vliet LJ, Tanke HJ, Vroljik H, Sloos WC: FISH and chips: Automation of fluorescent dot counting in interphase cell nuclei. Cytometry 28:1–10, 1997.
28. Niessen WJ, Vincken KL, Weickert JA, Viergever MA: Nonlinear multiscale representations for image segmentation. Comput Vision Image Understanding 66:233–245, 1997.
29. Rigaut JP, Vassy J, Herlin P, Duigou F, Masson E, Briane D, Foucrier J, Carvajal-Gonzalez S, Downs AM, Mandard A-M: Three-dimensional DNA image cytometry by confocal scanning laser microscopy in thick tissue blocks. Cytometry 12:511–524, 1991.
30. Rutovitz D: Data structures for operations on digital images. In: Pictorial Pattern Recognition. Thompson, Washington DC, 1968, pp 105–133.
31. Salari E, Siy P: The ridge-seeking method for obtaining the skeleton of digital images. IEEE Trans Syst Man Cybern 14:524–528, 1984.
32. Starink JPP, Gerbrands JJ: Three-dimensional object delineation by dynamic programming. Bioimaging 2:204–211, 1994.
33. Strasters KC, Smeulders AWM, Buijs M, Houtsmuller AB, Voort HTMvd, Nanninga NN: A 3-D model for chromatin organization of G1 and G2 populations from quantitative confocal image analysis. Cytometry 27:201–212, 1997.
34. Strasters KC, Voort HTMvd, Smeulders AWM: Fast attenuation correction in fluorescence confocal imaging: A recursive approach. Bioimaging 2:78–92, 1994.
35. Strasters KC, Gerbrands JJ: Three-dimensional image segmentation using a split, merge and group approach. Patt Rec Lett 12:307–322, 1991.
36. Thiran J-P, Macq B: Morphological feature extraction for the classification of digital images of cancerous tissues. IEEE Trans Biomed Engin 43:1011–1020, 1996.
37. Thompson CT, LeBoit PE, Nederlof PM, Gray JW: Thick-section fluorescence *in situ* hybridization on formalin-fixed, paraffin-embedded archival tissue provides a histogenetic profile. Am J Pathol 144:237–243, 1994.
38. Vincent L: Morphological grayscale reconstruction in image analysis: Applications and efficient algorithms. IEEE Trans Image Proc 2:176–201, 1993.
39. Wu H-S, Barra J: An efficient semi-automatic algorithm for cell contour extraction. J Microsc 179:270–276, 1995.
40. Zhu Q, Tekola P, Baak JPA, Beliën JAM: Measurement by confocal laser scanning microscopy of the volume of epidermal nuclei in thick skin sections. Analyt Quant Cytol Histol 16:145–152, 1994.

APPENDIX:

INSTRUCTIONS FOR OPERATING THE ALGORITHM

(1) Begin execution of the algorithm by entering the name of the algorithm followed by the file name of the 3D image for segmentation. The algorithm will provide a gray-scale display of the top xy plane of the nuclear counterstain component of the 3D image.

(2) Step down through the xy planes of the 3D image by clicking the right mouse button in the top half of the gray-scale display. (Step back up by clicking in the bottom half.) Stop at an xy plane that appears to pass through the center of the nucleus to be segmented (see plane abcd in Fig. 1A for an example).

(3) Drawing the first border. Using the left button, click at successive points around the edge of the object. The successive points will be joined by straight lines. Use the right button to undo actions of the left button. When you have almost completed the loop around the object, use the middle button to join the last point to the first.

(4) Drawing the second border. After a delay of about a second, the algorithm will display an orthogonal plane overlaid with a vertical yellow line. (The vertical yellow line is the edge-on view of the border drawn in the previous step; see plane efgh in Fig. 1B). Draw two successive loops around the object. The first starts at the top of the yellow line, proceeds with the object to the right of the direction of travel, and ends at the bottom of the yellow line. The second continues around the object in the same direction, starting at the bottom and ending at the top.

(5) Drawing the third border. Repeat the previous step (see plane ijkl in Fig. 1C).

(6) Drawing the fourth border. Repeat the previous step, except this time the yellow line is horizontal. Start at the left (see plane efgh in Fig. 1C).

(7) Drawing the fifth border. Repeat the previous step, except this time there is a vertical and a horizontal yellow line. Start at the top of the vertical line and proceed to the right end of the horizontal line. Continue in the same direction until the object has been circumnavigated (see plane abcd in Fig. 1C). At this point, the algorithm will take a few seconds to perform the interpolation and the surface optimization (if requested). The segmented object is blacked out in the 3D image so it cannot be accidentally segmented again.

(8) Continue from step 2 to segment more objects.